Dispersion Control in Plasmonic Open Nanocavities

Xinli Zhu, Jiasen Zhang,* Jun Xu, Heng Li, Xiaosong Wu, Zhimin Liao, Qing Zhao, and Dapeng Yu*

State Key Laboratory for Mesoscopic Physics, Department of Physics, Peking University, Beijing 100871, People's Republic of China

ABSTRACT We experimentally demonstrate the dependence of plasmonic resonant properties on cavity height in open circular cylinder nanocavities as a result of a strong three-dimensional confinement of the electromagnetic field, which shows a new way to tailor the dispersion of surface plasmon polaritons in cavities. The azimuthal and the axial symmetric plasmonic mode patterns are directly observed at resonant wavelengths using cathodoluminescence spectroscopy. Plasmonic modes and optical vertical cavity modes can be simultaneously excited and can coexist in a nanocavity with sufficient height. The highest quality factor, which is up to 73, is obtained in a 500 nm high cavity. The smallest mode volume is only 0.031 λ_{SPP}^3, and the corresponding Purcell factor is 71. Open nanocavities provide space for the interaction between an optical emitter and a confined electromagnetic field. Many applications can be expected, such as plasmonic light-emitting devices and nanolasers.

KEYWORDS: surface plasmon polaritons · red shift · cathodoluminescence · nanocavities · mode pattern

Surface plasmon polaritons (SPPs) are hybrid electromagnetic and free-electron collective oscillations evanescently bound at the interface between a metal and a dielectric,[1,2] which provides great potential to break the diffraction limit of light[3−5] and realize nanophotonic applications.[6−9] As a fundamental building block of future integrated optical circuits, plasmonic cavities, which offer the ability to confine an optical field in a small volume below the wavelength of light using metallic nanostructures, attract much attention.[10−13] Hao *et al*. observed the effects of structural symmetry breaking in a plasmonic cavity, consisting of a disk inside a thin ring, which supports superradiant and subradiant modes.[14] Mapping the electron-beam-excited full plasmonic mode in nanocavities using the EELS technique was report by Koh *et al*.[15] Hofmann *et al*. observed plasmonic modes of annular resonators in nanofabricated metal surfaces by cathodoluminescence (CL).[11] Recently, three-dimensional (3D) confinement of SPPs was realized in a nanosheet plasmon cavity, which was constructed *via* a metal−insulator−metal (MIM) structure.[16] In addition, disk resonators sustaining MIM SPPs were proposed to achieve a strong confinement of light and an ultrasmall mode volume.[17] In such MIM disk cavities, the transverse confinement of plasmonic resonant modes is supported by two enclosed metal layers. The plasmonic nanocavities are also an ideal platform to study the interaction between optical emitters, such as quantum dots and single molecules, and a confined electromagnetic field with Purcell-enhanced spontaneous emission because of the small mode volume. Therefore, open nanocavities are necessary to put different emitters into the cavities through open windows. Plasmonic resonant modes in two types of open plasmonic nanocavities were studied in our previous works.[18,19] Although the electric field of SPPs is evanescently perpendicular to the metal−dielectric interface and decays exponentially when at a distance from the surface, 3D confinement of SPPs in open nanocavities should crucially influence the plasmonic resonant properties. To date, there are no detailed studies on how resonant behavior and field confinement are impacted by cavity height perpendicular to the SPP propagation plane in 3D open nanocavities.

In this article, we systematically investigate the dependence of resonant wavelengths and plasmonic modes on cavity diameter and height in open circular cylinder nanocavities using CL spectroscopy. Plasmonic resonant wavelengths of the cavities exhibit considerable red shift with an increase in cavity height for the same cavity diameter and mode, even for relatively large cavities. The experimentally determined dispersion relation of SPPs demonstrates strong electromagnetic field confinement in the cavity with large cavity height. Monochromatic CL images taken at resonant wavelengths with nanoscale spatial resolution enable us to identify the symmetry and the order of the plasmonic modes in the nanocavities. The measured quality (Q) factors increase monotonically with an

* Address correspondence to jszhang@pku.edu.cn, yudp@pku.edu.cn.

Received for review May 25, 2011 and accepted July 12, 2011.

Published online July 12, 2011
10.1021/nn201916n

increase in cavity height for the same plasmonic mode. The largest *Q* factor is 73 at 697 nm in a 500 nm high cavity. Vertical cavity optical resonant modes (VCORMs) are also demonstrated in tall cavities.

RESULTS AND DISCUSSION

Silver plasmonic open circular cylinder nanocavities were fabricated using a template stripping method we previously developed and reported.[18] The cavity diameter, *D*, ranges from 290 to 860 nm, whereas the cavity height, *H*, is from 80 to 550 nm. Figure 1a and b show the top-view and 45°-tilted scanning electron microscopy (SEM) images of a typical open nanocavity with 750 nm diameter and 550 nm height. Atomic force microscope measurement shows that the root-mean-square roughness of the silver surface is better than 0.88 nm.[18] The fabrication method produces an ultrasmooth silver surface, a precipitous top-to-bottom profile, and an ideal geometry, which are crucial in investigating SPP behavior in nanocavities. The silver wall forms a whispering gallery for SPPs. The origin is set at the center of the undersurface, and the silver–air interface is the $z = 0$ plane.

A nanoscale open cavity needs an excitation method with a spatially resolved ability (~10 nm) to measure plasmonic mode patterns. The broad energy range of the fast focus electron beam can act as an effective and flexible plasmonic spot probe because of its unsurpassed spatial resolution compared with an optical detection method.[20–25] In the experiment, the excitation of SPPs and the collection of emitted spectra were performed using CL spectroscopy. A similar technique was used in previous reports on the study of plasmonics.[19–21]

A collection of CL spectra was obtained when the electron beam was impinged vertically at the center of the undersurface of the open nanocavities. Figure 2a–e show the CL spectra of nanocavities with heights of 80, 150, 250, 430, and 550 nm, respectively. The resonant peaks of the CL spectra can be sorted into several series indicated by dashed lines. In the same series, the resonant wavelengths shift to longer wavelengths with increasing cavity lengths and a fixed height, suggesting that plasmonic resonant wavelengths are strongly dependent on cavity size. Single or multimode SPPs can be chosen in the plasmonic cavity by changing the cavity diameter.

To determine the resonant modes, we directly imaged all of the plasmonic mode patterns at the resonant wavelengths using the monochromatic CL imaging mode. The CL image of a nanocavity, with a diameter (*D*) of 490 nm and a height (*H*) of 250 nm at a resonant wavelength of 698 nm, is shown in Figure 2f. Figure 2g–i are the typical monochromatic CL images for a cavity with a 765 nm diameter and a 250 nm height at resonant wavelengths of 681, 528, and 501 nm, respectively. These results show the azimuthal

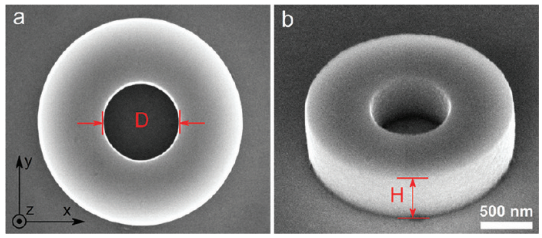

Figure 1. Plasmonic circular cylinder nanocavities: (a) top-view SEM image of a representative cavity with a 750 nm diameter and a 550 nm height; (b) 45°-tilted SEM image of the cavity.

and the axial symmetry patterns of the plasmonic modes in the nanocavities. In the same series, the resonant modes are also the same. In the experiment, the CL collection system with a parabolic reflector, which is asymmetric, was used to collect emitted light. The asymmetric detector results in symmetry breaking. Thus, we can obtain symmetric breaking patterns, even in a perfectly symmetric structure, in the spectral mapping CL.

To study the origin of the plasmonic modes, we used the finite-difference time-domain (FDTD) method to calculate the electric field intensity distribution of nanocavities that have the same geometry. Inasmuch as the electron beam locally excites the out-of-plane electric field component of SPPs in the cavity,[19] we calculated the plasmonic resonant mode patterns of the out-of-plane electric field component in the undersurface and show the results in Figure 2j–m. The axial asymmetry of the excited SPPs and the propagation loss induce slight distortions in the intensity compared with the experimental results. The features of the resonant mode patterns of the SPPs are completely reproduced by the numerical results. The simulation also demonstrates that the resonant wavelengths, indicated by the blue dashed lines, correspond to the plasmonic modes. The resonant modes, indicated by the green dashed lines in Figure 2d,e, are discussed later.

Here, we name the resonant modes as (*m*, *n*), where the integers *m* and *n* denote the azimuthal symmetry number relative to the rotational axis perpendicular to the nanocavity surface and the number of intensity antinodes of the out-of-plane electric field component in the radial direction, respectively. The plasmonic modes can be determined by combining the resonant mode patterns of the experimental and the numerical results. Thus, the plasmonic modes in Figure 2f and j, g and k, h and l, and i and m are assigned to the modes (0, 1), (1, 1), (2, 1), and (0, 2), respectively. On the basis of these results, we can identify the plasmonic modes of the four series of resonant wavelengths indicated by the blue dashed lines with the blue characters (Figure 2a–e).

To show clearly the dependence of SPP confinement on cavity height, the resonant wavelengths, as a function of cavity diameter, with the cavity heights increasing from 80 to 550 nm for the plasmonic modes (0, 1)

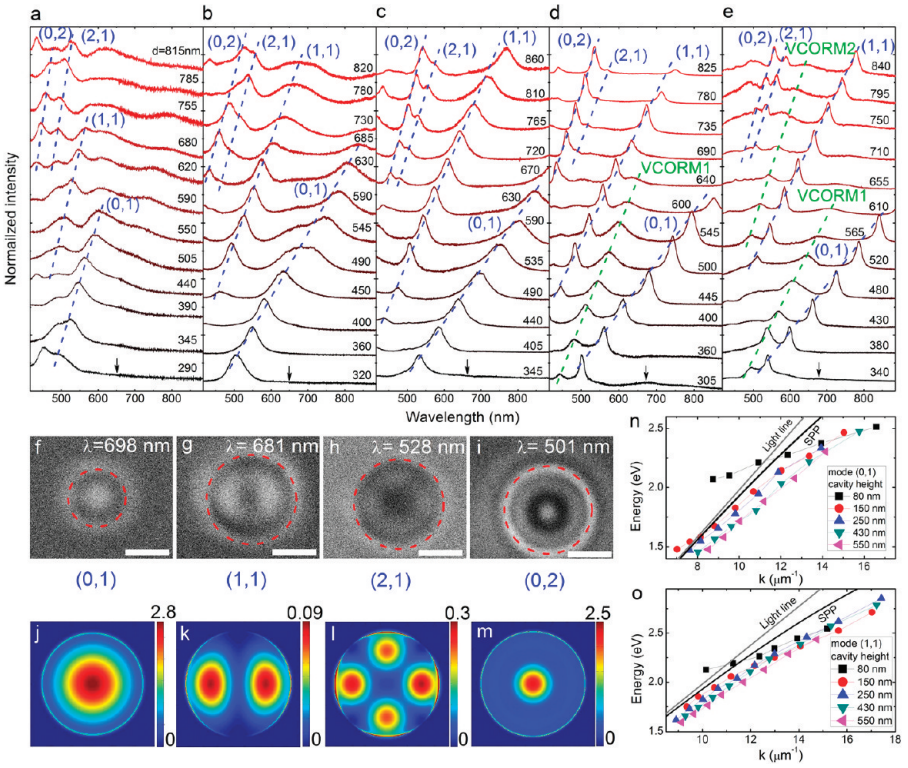

Figure 2. CL spectra and mode patterns of the plasmonic nanocavities. (a−e) CL spectra of nanocavities with 80, 150, 250, 430, and 550 nm heights, respectively. The numbers on the right side of the figures indicate the diameters of the cavities in nm. The spectra were obtained when the electron beam was incident near the centers of the cavities. The plasmonic modes are classified and indicated with blue dotted lines and characters, respectively. Spectra are offset vertically for clarity. (f) Typical monochromatic CL image at a resonant wavelength of 698 nm for a cavity with a 490 nm diameter. (g−i) Typical monochromatic CL images at resonant wavelengths of 681, 528, and 501 nm for a cavity with a 765 nm diameter, respectively. The red dashed circles show the boundaries of the cavities. Scale bars are 500 nm. (j−m) Calculated intensity patterns of the out-of-plane electric components for the plasmonic modes (0, 1), (1, 1), (2, 1), and (0, 2), respectively. (n, o) Dispersions of plasmonic modes (0, 1) and (1, 1) in the nanocavities. The gray and black lines respectively represent the dispersions of light in a vacuum and SPPs on an infinite Ag film.

and (1, 1) are plotted in Figure S1a and b, respectively (Supporting Information). The resonant wavelength of the same plasmonic mode significantly red shifts to a longer wavelength for increasing cavity height. For instance, we clearly observed that the resonant wavelength red shifts from 600 to 744, 764, 797, and 821 nm in 550 nm diameter cavities for plasmonic mode (0, 1) when the height of the cavities is increased from 80 to 150, 250, 430, and 550 nm, respectively. The red shift is most obvious when the cavity height is increased from 80 to 150 nm for larger wavelengths, where the decay length of SPPs in the air is larger than 150 nm.

If the reflection phase shift is assumed to be π, the effective SPP wavelength for resonant mode (m, n) is $\lambda_{SPP} = D\pi/x_{mn}$, where x_{mn} is the nth root of the Bessel function $J_m(x) = 0$, according to the resonant condition of a cylindrical metal cavity in the radiowave or microwave regime.[26] On the basis of the data from Figure 2a−e, we can obtain the dispersion relation of the SPPs in the cavity, which is a crucial parameter to evaluate the performance of the cavity. Figure 2n and o respectively show the dispersion relation of plasmonic modes (0, 1) and (1, 1) with the cavity heights increasing from 80 to 550 nm. Most of the data are on the right-hand side of the dispersion of SPPs on an infinite Ag film, which indicates that nanocavities with larger cavity height have stronger electromagnetic field confinement and the cavity height is an important factor in controlling the dispersion of SPPs in an open nanocavity. Such a 3D subwavelength confinement of SPPs also tailors the interaction between the electromagnetic field and the optical emitter in the cavity. For example, a previous study[27] shows that cylindrical plasmonic core−shell resonators can effectively modify the local density of the optical states and dramatically enhance the radiative decay rate.

However, the dispersion data for low cavity height and long wavelength in Figure 2n and o are on the left-hand side of the dispersion of SPPs on an infinite Ag film, which means that the effective wavelength is overestimated. This can be attributed to the reflection phase shift largely deviating from π for low cavity height because the penetration depth of SPPs into the air is much larger than the cavity height.

The cavity height is a key parameter for the confinement of an electromagnetic field in the cavity. We calculated the plasmonic field intensity patterns of (0, 1) modes in the $y = 0$ plane for circular cylinder

cavities with a constant diameter of 550 nm and cavity heights of 80, 150, 250, 430, and 550 nm (Supporting Information, Figure S2a–e). For low cavity heights, the electromagnetic field overflows from the cavity and the confinement along the *x* direction is low. For large cavity heights, the electromagnetic field is tightly confined in the cavity, which induces the red shift of the resonant wavelength.

In Figure 2a–e, we notice that a new series of resonant wavelengths, which are marked by the green dashed line, show up in 430 and 550 nm high cavities. These resonant wavelengths cannot be explained using plasmonic resonant modes. Figure 3a shows a typical monochromatic CL image at a wavelength of 545 nm for a cavity that is 445 nm in diameter and 430 nm in height. The FDTD simulation demonstrates that these modes originate from the optical vertical cavities. In the simulation, a pulsed plane wave with *x*-polarization was incident into the cavity, from the $z = 0$ plane along the *z*-axis. The resonant intensity patterns at the resonant wavelength of 521 nm in the $z = 0$ and $y = 0$ planes corresponding to the case in Figure 3a are shown in Figure 3b and c, respectively. A tall cavity is also a metal optical circular cylinder cavity, in which VCORMs appear. Here, the open window acts as an air reflector, which has a different reflection phase shift than that of the silver reflector. At a height of 430 nm, just the lowest order VCORM exists in Figure 2d. When the height increases to 550 nm, a higher order VCORM appears. Furthermore, we calculate the plasmonic mode (0, 1) patterns at the resonant wavelength of 658 nm in the $y = 0$ plane for the same cavity size and show the result in Figure 3d. Although the plasmonic (0, 1) mode and the VCORM have very similar intensity profiles in the $z = 0$ plane, their resonant behaviors are complete different. The VCORMs are radiant modes with a broader band other than the subradiant plasmonic modes. Fano resonances may occur when the VCORMs and plasmonic modes are overlapped by the adjustment of the geometry of the cavity.

The cavity *Q* factor, which is defined as the resonant frequency/bandwidth (or approximately resonant wavelength/full width at half-maximum) of the cavity resonance, is a measure of the ratio of optical energy stored in the nanocavity to the cycle-average power radiated out of the cavity. We directly obtain the *Q* factors from Figure 2a–e and show the *Q* factors of various plasmonic and optical modes in the 550 nm high cavities in Figure 4a. The *Q* factors of the plasmonic modes are obviously larger than that of the VCORMs due to the high reflectivity of the silver reflector. On the other hand, the air reflector at the top surface of the cavity for VCORMs has a relatively small reflectivity. As a result, the measurement of the *Q* factor of the cavity provides an effective method for distinguishing between the plasmonic and the optical modes in such a cavity. The *Q* factor of the plasmonic

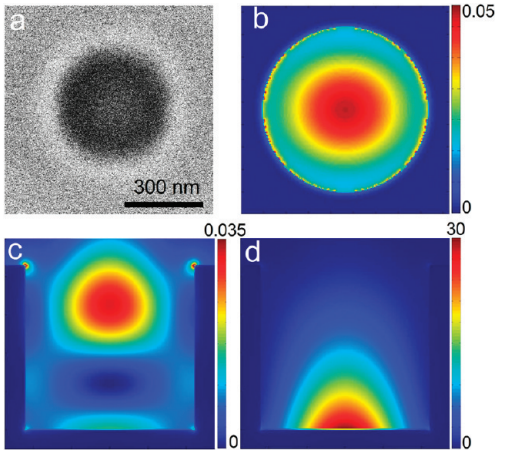

Figure 3. VCORM and plasmonic mode of a circular cylinder cavity with a 445 nm diameter and a 430 nm height. (a) Typical monochromatic CL image at a wavelength of 545 nm. (b, c) Calculated VCORM field intensity patterns at the resonant wavelength of 521 nm in the $z = 0$ and $y = 0$ planes, respectively, for the same mode as (a). (d) Calculated plasmonic mode field intensity patterns at the resonant wavelength of 658 nm in the $y = 0$ plane.

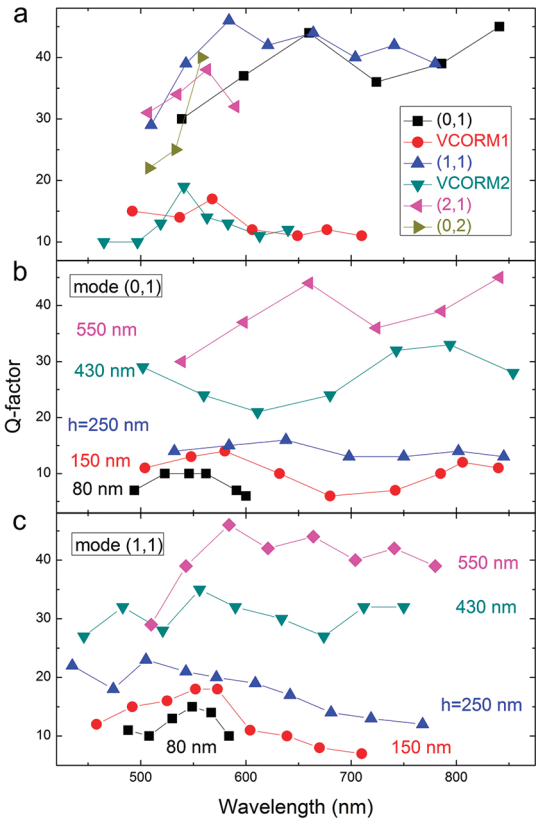

Figure 4. *Q* factors directly obtained from the measured CL spectra. (a) *Q* factors of the 550 nm high nanocavities with increasing cavity diameters for various plasmonic and optical modes. (b, c) *Q* factors of the nanocavities with increasing cavity heights, from 80 to 550 nm, for modes (0, 1) and (1, 1), respectively.

mode depends on the reflectivity of the reflectors and the propagation loss of the SPPs for a fixed cavity height. The low *Q* factor of a short wavelength is attributed to

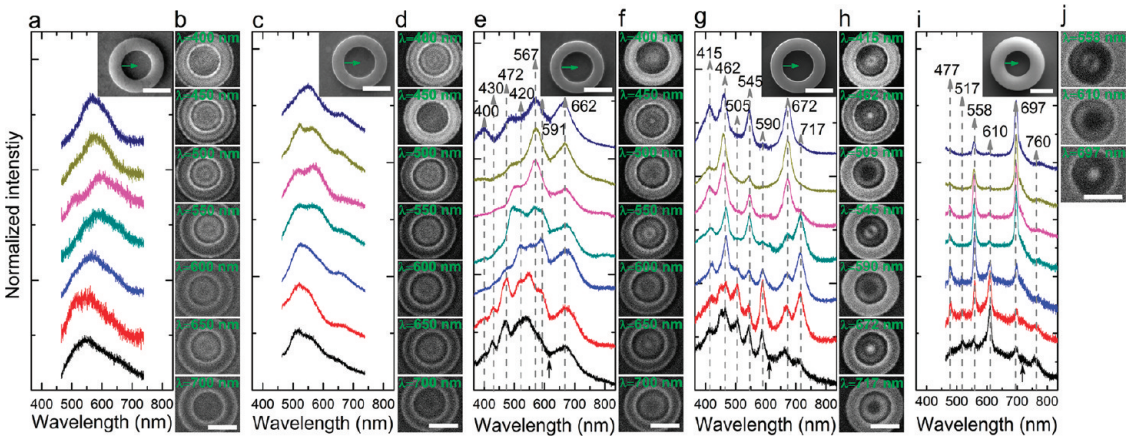

Figure 5. CL spectra and mode patterns of the plasmonic ring nanocavities with constant cavity diameter of 1140 nm. (a, c, e, g, and i) Line-scanning CL spectra of 7 nanocavities with 50, 80, 150, 300, and 500 nm heights, respectively. The electron beam excited from the side to the center of the cavity, with a step size of 95 nm, is indicated with green arrows in the inset SEM images (bottom = edge; top = center). Spectra are offset vertically for clarity. (b, d, f, h, and j) Monochromatic CL images at the indicated wavelengths. Scale bars are 1000 nm.

high propagation loss. Figure 4b and c show *Q* factors as a function of resonant wavelengths for plasmonic modes (0, 1) and (1, 1), respectively, with an increase in cavity heights, from 80 to 550 nm. The highest *Q* factor can go up to 46 at a resonant wavelength of 584 nm for a 550 nm high cavity, which represents a trade-off between the reflectivity of the silver reflector and the propagation loss. At the same time, the smallest *Q* factor is 6, at a resonant wavelength of 600 nm for an 80 nm high cavity.

A very small mode volume can be expected for the nanoscale size of the cavities and strong 3D confinement of the plasmonic resonant modes. The plasmonic field distributions in the $x-y$ plane are Bessel functions, and the field confinement distribution in the z direction follows the exponential decay of SPPs. For the (0, 1) mode, according to a simple analytical model with an approximation reflection phase shift of π and the definition of the mode volume, V,[12,28] we can evaluate the nanocavity's mode volume. For example, for a 305 nm diameter cavity, the resonant wavelength in a vacuum is 502 nm, and a mode volume $V = 0.031\ \lambda_{SPP}^3 = 0.0021\ \mu m^3$ can be obtained. Combining the experimental *Q* factor of 29 for the cavity, we can find the Purcell factor[29] is 71. Because of the relatively high Purcell factor and the character of the open nanocavities, they can be considered for use in spontaneous emission-enhancement optical devices and lasing.

To further investigate how the cavity height impacts the performance of the open nanocavity, cavities with a constant diameter, a diameter of 1140 nm, and various heights were fabricated. The electron beam was scanned from the side to the center of the cavity with a step size of 95 nm, as indicated by the green arrows in the SEM images (insets in Figure 5), and the collected CL spectra at each position of the cavities with 50, 80, 150, 300, and 500 nm heights are shown in Figure 5a, c, e, g, and i, respectively. There are only one or two indeterminate broad peaks for 50 and 80 nm high cavities in the measurement range, whereas there are 7, 7, and 6 distinct resonant wavelengths for 150, 300, and 500 nm high cavities, respectively. Obviously, the full width at half-maximum of the resonance reduces with an increase in cavity height. This means that a large cavity with a relatively low height cannot sufficiently support a plasmonic resonance because of the large propagation loss and the relatively small reflectivity. In such a large cavity, the cavity height still influences the resonant wavelength. For example, the resonant wavelengths red shift from 662 to 672 and 697 nm for the same mode, when the heights of the cavity are increased from 150 to 300 and 500 nm, respectively. Monochromatic CL images of cavities with 50, 80, and 150 nm heights were taken respectively at wavelengths between 400 and 800 nm with a 50 nm interval (Figure 5b, d, and f), whereas monochromatic CL images of cavities with 300 and 500 nm heights were obtained at the resonant wavelengths of the CL spectra (Figure 5h and j). Higher-order plasmonic modes appeared in the large cavities. The cavity with the 300 nm height provides the most abundant and clear plasmonic mode patterns, although the 500 nm high cavity results in a higher *Q* factor, which is as high as 73 at a resonant wavelength of 697 nm. Some mode patterns in the 500 nm high cavity could not be obtained despite the appearance of clear resonant peaks in the CL spectra. This may be attributed to the weak scattering of the SPPs at the upper corner of the silver wall in such a high cavity, which results in a low signal intensity collected by the CL microscope.

Unlike nanocrosses, in which the rotational symmetry has a crucial influence on the coupling between the SPPs and radiation,[30] the shape or rotational symmetry of the nanocavities determines only the plasmonic mode patterns and the modes are all subradiant because

the electromagnetic field is confined in the cavity. The experiment results also reveal that the nanocavities with different shapes should have the same dependence of the resonant wavelength, SPP dispersion, and *Q* factors on the cavity height. The different mechanism of the VCORMs from the plasmonic modes results in the different dependence of the resonant wavelength, dispersion, and *Q* factors on the cavity height, which gives a new way to manipulate the interaction between the VCORMs and plasmonic modes.

CONCLUSIONS

In summary, we have demonstrated the dependence of the resonant wavelength and the dispersion of SPPs on cavity height in open plasmonic nanocavities, which is caused by the tight 3D confinement of the plasmonic electromagnetic field. The plasmonic modes are directly obtained and assessed by spatially and spectrally resolved CL. The experimental results reveal effective modulation of the dispersion of SPPs using the height of metal walls in open nanocavities. This phenomenon is of importance to the study on the interaction between an open nanocavity and optical emitters. The cavity also acts as an optical vertical cavity with an air window. VCORMs were demonstrated in tall cavities. The coexisting plasmonic and optical modes can be simply distinguished by means of the *Q* factor. The plasmonic resonant modes show a high *Q* factor, which benefits from the high reflectivity of the silver reflectors. A *Q* factor as high as 73 was obtained in the cavity with a 1140 nm diameter and a 500 nm height. The plasmonic open nanocavities are ideal candidates that can be used to realize plasmonic nanodevices, such as efficient light-emitting devices,[31] cavity quantum electrodynamics, and plasmonic nanolasers,[4] as well as fundamental elements of plasmonic circuit networks.[32]

METHODS

Fabrication of Metal Nanocavities. A poly(methyl methacrylate) (PMMA) film with desired thickness was spun on a silicon wafer and then exposed and developed into designed nanostructures *via* electron beam lithography (EBL). A silver layer with thickness larger than the PMMA layer was then deposited on the negative patterns by magnetron sputtering deposition. After being glued to another silicon substrate with an epoxy resin adhesive, the metal layer was easily stripped off from the PMMA surface due to the weak adhesion between the metal layer and the PMMA. After cleansing the residual PMMA with acetone, the resulting top metal layer inherited completely the morphology and the smoothness of the PMMA patterns.

EBL and Characterization. EBL was performed using SEM equipped with a lithography attachment (Raith Elphy Plus). The morphology of the fabricated patterns was characterized by SEM (FEI company, DB235and Quanta 200F).

CL Measurements. Spatially and spectrally resolved CL measurements and CL imaging of the plasmonic modes of the nanocavities were carried out by combining an SEM (FEI Quanta 200F) and a CL (Gatan Mono CL 3+) detection system. We excited SPPs on the undersurface of the cavities using a 30 keV focus electron beam with a beam diameter of ~5 nm. A parabolic reflector with an off-axis focus, mounted above a sample holder, was used to collect emitted light. In the single-point spectroscopy collecting mode, the electron beam was fixed at a point on the undersurface. Emitted light was coupled through a grating monochromator and then recorded by a charge-coupled device array detector. In the experiment, all the CL spectra were collected at an acquisition time of 16 s. In the monochromatic CL imaging mode, the electron beam homogeneously scanned over a chosen area of the cavity in a scanning mode of operation. Light was coupled through the grating monochromator, such that a selected wavelength with a 30 nm spectral passband, at a resonant wavelength, for example, reached the photomultiplier tube detector. Therefore, monochromatic and SEM images can be acquired synchronously. In the present study, any drift in the scanning process of the CL images is not corrected. Inasmuch as the emission spectra collected include transition radiation emission[33,34] and light decoupled from the SPPs, the measured CL spectra were corrected by subtracting the background emission spectra of unstructured Ag obtained far from the structured Ag sampling area.

Calculations. The simulations are obtained with a commercial FDTD solver (Lumerical FDTD solution 7.0) using a mesh of 2 nm and perfectly matched layers as simulation boundaries. A Drude model is locally fitted to experimentally obtained optical constants of Ag.[35] Since the plasmonic modes do not depend on the excitation source of SPPs, in the simulation, a light pulse was used to excite the SPPs. The *x*-polarized pulse was incident onto the right-hand side boundary of the cavity from the $z = 0$ plane along the *z*-axis, to ensure both symmetric and asymmetric modes, with respect to the *y*-axis, which could be excited. Then, the SPPs oscillated freely to form the plasmonic patterns. For the simulation of the VCORM, an *x*-polarized light pulse was incident into the cavity along the $-z$ direction from the upper side.

Acknowledgment. This work was supported by the NSFC (Nos. 61036005, 11074015, and 11023003) and the National 973 Program of China (No. 2009CB623703), MOST.

Supporting Information Available: Resonant wavelengths as a function of cavity diameters with increasing cavity heights, and normalized intensity profiles of the calculated plasmonic modes. This material is available free of charge via the Internet at http://pubs.acs.org.

REFERENCES AND NOTES

1. Raether, H. *Surface Plasmons on Smooth and Rough Surfaces and on Gratings*; Springer: Berlin, 1988.
2. Barnes, W. L.; Dereux, A.; Ebbesen, T. W. Surface Plasmon Subwavelength Optics. *Nature* **2003**, *424*, 824–830.
3. Maier, S. A.; Kik, P. G.; Atwater, H. A.; Meltzer, S.; Harel, E.; Koel, B. E.; Requicha, A. A. G. Local Detection of Electromagnetic Energy Transport below the Diffraction Limit in Metal Nanoparticle Plasmon Waveguides. *Nat. Mater.* **2003**, *2*, 229–232.
4. Oulton, R. F.; Sorger, V. J.; Zentgraf, T.; Ma, R. M.; Gladden, C.; Dai, L.; Bartal, G.; Zhang, X. Plasmon Lasers at Deep Subwavelength Scale. *Nature* **2009**, *461*, 629–632.
5. Bozhevolnyi, S. I.; Volkov, V. S.; Devaux, E.; Laluet, J. Y.; Ebbesen, T. W. Channel Plasmon Subwavelength Waveguide Components Including Interferometers and Ring Resonators. *Nature* **2006**, *440*, 508–511.

6. Luk'yanchuk, B.; Zheludev, N. I.; Maier, S. A.; Halas, N. J.; Nordlander, P.; Giessen, H.; Chong, C. T. The Fano Resonance in Plasmonic Nanostructures and Metamaterials. *Nat. Mater.* **2010**, *9*, 707–715.
7. Walters, R. J.; van Loon, R. V. A.; Brunets, I.; Schmitz, J.; Polman, A. A Silicon-Based Electrical Source of Surface Plasmon Polaritons. *Nat. Mater.* **2010**, *9*, 21–25.
8. Falk, A. L.; Koppens, F. H. L.; Yu, C. L.; Kang, K.; Snapp, N. D.; Akimov, A. V.; Jo, M. H.; Lukin, M. D.; Park, H. Near-Field Electrical Detection of Optical Plasmons and Single-Plasmon Sources. *Nat. Phys.* **2009**, *5*, 475–479.
9. Atwater, H. A.; Polman, A. Plasmonics for Improved Photovoltaic Devices. *Nat. Mater.* **2010**, *9*, 205–213.
10. Lal, S.; Link, S.; Halas, N. J. Nano-Optics from Sensing to Waveguiding. *Nat. Photonics* **2007**, *1*, 641–648.
11. Hofmann, C. E.; Vesseur, E. J. R.; Sweatlock, L. A.; Lezec, H. J.; García de Abajo, F. J.; Polman, A.; Atwater, H. A. Plasmonic Modes of Annular Nanoresonators Imaged by Spectrally Resolved Cathodoluminescence. *Nano Lett.* **2007**, *7*, 3612–3617.
12. Sorger, V. J.; Oulton, R. F.; Yao, J.; Bartal, G.; Zhang, X. Plasmonic Fabry-Perot Nanocavity. *Nano Lett.* **2009**, *9*, 3489–3493.
13. Vesseur, E. J. R.; García de Abajo, F. J.; Polman, A. Modal Decomposition of Surface-Plasmon Whispering Gallery Resonators. *Nano Lett.* **2009**, *9*, 3147–3150.
14. Hao, F.; Sonnefraud, Y.; Dorpe, P. V.; Maier, S. A.; Halas, N. J.; Nordlander, P. Symmetry Breaking in Plasmonic Nanocavities: Subradiant LSPR Sensing and a Tunable Fano Resonance. *Nano Lett.* **2008**, *8*, 3983–3988.
15. Koh, A. L.; Fernández-Domínguez, A. I.; McComb, D. W.; Maier, S. A.; Yang, J. K. W. High-Resolution Mapping of Electron-Beam-Excited Plasmon Modes in Lithographically Defined Gold Nanostructures. *Nano Lett.* **2011**, *11*, 1323–1330.
16. Miyazaki, H. T.; Kurokawa, Y. Squeezing Visible Light Waves into a 3-nm-Thick and 55-nm-Long Plasmon Cavity. *Phys. Rev. Lett.* **2006**, *96*, 097401.
17. Kuttge, M.; García de Abajo, F. J.; Polman, A. Ultrasmall Mode Volume Plasmonic Nanodisk Resonators. *Nano Lett.* **2010**, *10*, 1537–1541.
18. Zhu, X.; Zhang, Y.; Zhang, J.; Xu, J.; Ma, Y.; Li, Z.; Yu, D. Ultrafine and Smooth Full Metal Nanostructures for Plasmonics. *Adv. Mater.* **2010**, *22*, 4345–4349.
19. Zhu, X. L.; Ma, Y.; Zhang, J. S.; Xu, J.; Wu, X. F.; Zhang, Y.; Han, X. B.; Fu, Q.; Liao, Z. M.; Chen, L.; *et al*. Confined Three-Dimensional Plasmon Modes inside a Ring-Shaped Nanocavity on a Silver Film Imaged by Cathodoluminescence Microscopy. *Phys. Rev. Lett.* **2010**, *105*, 127402.
20. Bashevoy, M. V.; Jonsson, F.; Krasavin, A. V.; Zheludev, N. I.; Chen, Y.; Stockman, M. I. Generation of Traveling Surface Plasmon Waves by Free-Electron Impact. *Nano Lett.* **2006**, *6*, 1113–1115.
21. van Wijngaarden, J. T.; Verhagen, E.; Polman, A.; Ross, C. E.; Lezec, H. J.; Atwater, H. A. Direct Imaging of Propagation and Damping of Near-Resonance Surface Plasmon Polaritons Using Cathodoluminescence Spectroscopy. *Appl. Phys. Lett.* **2006**, *88*, 221111.
22. García de Abajo, F. J. Optical Excitations in Electron Microscopy. *Rev. Mod. Phys.* **2010**, *82*, 209.
23. Cai, W.; Sainidou, R.; Xu, J. J.; Polman, A.; García de Abajo, F. J. Efficient Generation of Propagating Plasmons by Electron Beams. *Nano Lett.* **2009**, *9*, 1176–1181.
24. Gomez-Medina, R.; Yamamoto, N.; Nakano, M.; García de Abajo, F. J. Mapping Plasmons in Nanoantennas via Cathodoluminescence. *New J. Phys.* **2008**, *10*, 105009.
25. Vesseur, E. J. R.; de Waele, R.; Kuttge, M.; Polman, A. Direct Observation of Plasmonic Modes in Au Nanowires Using High-Resolution Cathodoluminescence Spectroscopy. *Nano Lett.* **2007**, *7*, 2843–2846.
26. Jackson, J. D. *Classical Electrodynamics*; Wiley: New York, 1999.
27. Hofmann, C. E.; García de Abajo, F. J.; Atwater, H. A. Enhancing the Radiative Rate in III−V Semiconductor Plasmonic Core−Shell Nanowire Resonators. *Nano Lett.* **2011**, *11*, 372–376.
28. Foresi, J. S.; Villeneuve, P. R.; Ferrera, J.; Thoen, E. R.; Steinmeyer, G.; Fan, S.; Joannopoulos, J. D.; Kimerling, L. C.; Smith, H. I.; Ippen, E. P. Photonic-Bandgap Microcavities in Optical Waveguides. *Nature* **1997**, *390*, 143–145.
29. Purcell, E. *Proceedings of the American Physical Society*. *Phys. Rev.* **1946**, *69*, 681.
30. Verellen, N.; Van Dorpe, P.; Vercruysse, D.; Vandenbosch, G. A. E.; Moshchalkov, V. V. Dark and Bright Localized Surface Plasmons in Nanocrosses. *Opt. Express* **2011**, *19*, 11034–11051.
31. Akimov, A.; Mukherjee, A.; Yu, C.; Chang, D.; Zibrov, A.; Hemmer, P.; Park, H.; Lukin, M. Generation of Single Optical Plasmons in Metallic Nanowires Coupled to Quantum Dots. *Nature* **2007**, *450*, 402–406.
32. Ebbesen, T. W.; Genet, C.; Bozhevolnyi, S. I. Surface-Plasmon Circuitry. *Phys. Today* **2008**, *61*, 44–50.
33. Leveque, G.; Olson, C. G.; Lynch, D. W. Reflectance Spectra and Dielectric Functions for Ag in the Region of Interband-Transitions. *Phys. Rev. B* **1983**, *27*, 4654–4660.
34. Fuster, G.; Tyler, J. M.; Brener, N. E.; Callaway, J.; Bagayoko, D. Electronic-Structure and Related Properties of Silver. *Phys. Rev. B* **1990**, *42*, 7322–7329.
35. Palik, E. D. *Handbook of Optical Constants of Solids*; Academic Press: Orlando, FL, 1985.